Check for updates

ADVANCED FUNCTIONAL MATERIALS
www.afm-journal.de

$TaCo_2Te_2$: An Air-Stable, High Mobility Van der Waals Material with Probable Magnetic Order

*Ratnadwip Singha, Fang Yuan, Guangming Cheng, Tyger H. Salters, Yuzki M. Oey, Graciela V. Villalpando, Milena Jovanovic, Nan Yao, and Leslie M. Schoop**

Van der Waals (vdW) materials are an indispensable part of functional device technology due to their versatile physical properties and ease of exfoliating to the low-dimensional limit. Among all the compounds investigated so far, the search for magnetic vdW materials has intensified in recent years, fueled by the realization of magnetism in 2D. However, metallic magnetic vdW systems are still uncommon. In addition, they rarely host high-mobility charge carriers, which is an essential requirement for high-speed electronic applications. Another shortcoming of 2D magnets is that they are highly air sensitive. Using chemical reasoning, $TaCo_2Te_2$ is introduced as an air-stable, high-mobility, magnetic vdW material. It has a layered structure, which consists of Peierls distorted Co chains and a large vdW gap between the layers. It is found that the bulk crystals can be easily exfoliated and the obtained thin flakes are robust to ambient conditions after 4 months of monitoring using an optical microscope. Signatures of canted antiferromagntic behavior are also observed at low-temperature. $TaCo_2Te_2$ shows a metallic character and a large, nonsaturating, anisotropic magnetoresistance. Furthermore, the Hall data and quantum oscillation measurements reveal the presence of both electron- and hole-type carriers and their high mobility.

1. Introduction

Van der Waals (vdW) materials are the important building blocks of low-dimensional device technology as they provide the flexibility of designing a large number of unique heterostructures by stacking 2D atomic layers.[1] These layers can be chosen from an expansive catalogue of predicted vdW compounds[2] with different experimentally verified functionalities ranging from superconductivity[3,4] and metallic or semiconducting transport,[5,6] to optical properties[7,8] and magnetism.[9] Such assembled structures offer capabilities to manipulate the properties of different layers, for example, the proximity effect often leads to new quantum states at the interfaces.[10,11]

Out of all the vdW systems studied so far, magnetic vdW compounds have been of particular interest due to the discovery of the long-sought 2D magnetism and its high tunability.[12–20] 2D magnets have various technological applications, particularly in magnetic tunnel junctions.[21,22] In spite of such intense demand, the examples of true magnetic vdW materials (i.e., exfoliable down to few atomic layers) are rather limited. Moreover, almost all of them show either semiconducting or insulating electronic transport properties. Exceptions include metallic ferromagnets Fe_3GeTe_2,[23] Fe_4GeTe_2[24] and antiferromagnets RTe_3 (R = rare earth).[25–28] Among these, $GdTe_3$ has been highlighted for its high-mobility charge carriers that can play an important role in ultrafast, low-power electronics.[29] The only comparable high-mobility vdW systems are nonmagnetic graphite[30] and black phosphorus,[31] both of which have demonstrated their versatility in device fabrication.[32–36] Of course, graphite has shown many more interesting features especially generated by the Moiré pattern in twisted multilayer graphene,[37,38] including a novel ferromagnetic state in twisted bilayer graphene.[39] With intrinsic magnetism as another controllable parameter, $GdTe_3$ is a prime material candidate for spintronics applications[40] or creating twisted multilayer devices with magnetic order and metallic conductivity. However, one major limitation of this compound (and also the RTe_3 family in general) is its robustness, as the exfoliated $GdTe_3$ flakes degrade quickly after a brief exposure to air.[27] This introduces additional complexities during handling such as inert atmosphere exfoliation and encapsulation, as well as hinders its wide-scale use. An air-stable, high-mobility, magnetic vdW compound is therefore highly desired.

To design such a material, it helps to first understand the other high-mobility vdW magnet, $GdTe_3$. Its structure contains Te square-nets that are susceptible to a Peierls distortion, which results in the formation of a charge density wave (CDW). The

R. Singha, F. Yuan, T. H. Salters, G. V. Villalpando, M. Jovanovic, L. M. Schoop
Department of Chemistry
Princeton University
Princeton, NJ 08544, USA
E-mail: lschoop@princeton.edu
G. Cheng, N. Yao
Princeton Institute for Science and Technology of Materials
Princeton University
Princeton, NJ 08544, USA
Y. M. Oey
Materials Department and Materials Research Laboratory
University of California
Santa Barbara, CA 93106, USA
The ORCID identification number(s) for the author(s) of this article can be found under https://doi.org/10.1002/adfm.202108920.

DOI: 10.1002/adfm.202108920

 © 2021 Wiley-VCH GmbH

square-net motif has previously been linked to high electronic mobility, as it contains delocalized, hypervalent bonds.[41] Electron delocalization is often in competition with a Peierls distortion or a CDW; the distortion (partially) localizes these. Nonetheless, the partial delocalization can remain after the distortion, which is why the presence of a Peierls instability can be a good indicator for high mobility charge carriers.[42] Black phosphorus, for example has a distorted structure,[43] whereas in graphene such distortion is prevented by the delocalized electrons.[44] Using this chemical intuition, we searched for a layered material that exhibits a Peierls distortion in addition to magnetic species. $TaCo_2Te_2$ had been reported in a distorted layered structure and contains Co, thus fulfilling all the chemical requirements. We here show that it indeed features magnetism, high mobility, and can be exfoliated. Optical microscopy images show that the exfoliated flakes are stable in air for months.

2. Results and Discussions

2.1. Crystal Structure and Exfoliation of the Bulk Sample

The scanning electron microscope (SEM) image of a $TaCo_2Te_2$ single crystal is shown in Figure S1, Supporting Information. The energy dispersive X-ray spectroscopy (EDX) analysis on different regions of the crystal reveals almost ideal stoichiometry (Figure S2, Supporting Information). Single crystal X-ray diffraction (SCXRD) confirms the previously reported structure.[45] **Figure 1**a displays a typical indexed precession diffraction image. All the parameters related to the structural solution are summarized in Tables S1–S3 Supporting Information. The corresponding structure is presented in Figure 1b. $TaCo_2Te_2$ crystallizes in a layered orthorhombic structure with spacegroup *Pmcn* (62). The structure consists of quintuple layers that are stacked along the crystallographic *c*-axis and only held together by weak vdW forces (Figure 1b). Each quintuple layer consists of a puckered square-net layer of Ta atoms (Figure 1c) in the center, sandwiched by square-net layers of Co dimers, which again are sandwiched by Te layers. The Co dimers are tilted alternately with respect to the Ta square-net (Figure 1c). The Te atoms occupy the spaces in between the Ta and Co square-nets. The structure is distorted in respect to similar compounds such as $TaNi_2Te_2$;[46] the distortion becomes apparent if viewed along the *a*-axis. When the Ta atoms are ignored for a moment, one can see that the quintuple layer contains a pair of cobalt-tellurium zigzag chains, where the Co–Co distance alternates within every chain (Figure 1d). This Peierls distortion appears due to the structural instability in the quasi 1D zigzag chains. Peierls distortions often lead to the formation of a CDW in a material.[47] In $TaCo_2Te_2$, however, we have not observed any indications of a higher symmetry structure in SCXRD experiments up to 390 K.

While the vdW gap in the crystal structure suggests that exfoliation of this material should be possible, in reality, exfoliation often can be hindered by defects that occupy the gap.[48] In addition, while $TaCo_2Te_2$ is listed in the ICSD, it does not appear as an exfoliable material in the 2D materials database,[2] where materials were screened computationally for their exfoliation capability. To elucidate whether the vdW gap is large and free of defects, we studied the crystals with atomic-resolution high-angle annular dark-field scanning transmission electron microscopy (HAADF-STEM). In **Figure 2**a, the HAADF-STEM image of a $TaCo_2Te_2$ crystal viewed along the *a*-axis clearly demonstrates the large vdW gap between the layers. Using the images, we could calculate the vdW gap to be ≈0.314 nm. This value is higher than that for graphite and *h*-BN, as well as for the extensively studied transition metal dichalcogenides.[49] Thus, it should be possible to exfoliate the $TaCo_2Te_2$ crystals down to very thin flakes or even monolayers. Remarkably, the atomic-resolution elemental mapping, shown in Figure 2b, directly visualizes the Peierls distortion along the Co chains. The inset of Figure 2b shows an enlarged view with the consecutive Co atoms highlighted by white points. We determined that the distance changes from ≈2.82 to ≈4.02 Å between alternate Co–Co atomic pairs within a chain. These values are in agreement with the X-ray diffraction data [2.552(4) and 4.019(4) Å]. The obtained selected area electron diffraction pattern in Figure 2c matches well with the simulated pattern from the reported crystal structure and confirms the high crystalline quality of the grown $TaCo_2Te_2$ samples.

To investigate the viability of using $TaCo_2Te_2$ in low-dimensional devices, we exfoliated the single crystals mechanically using Scotch Tape and transferred the flakes on a silicon wafer.

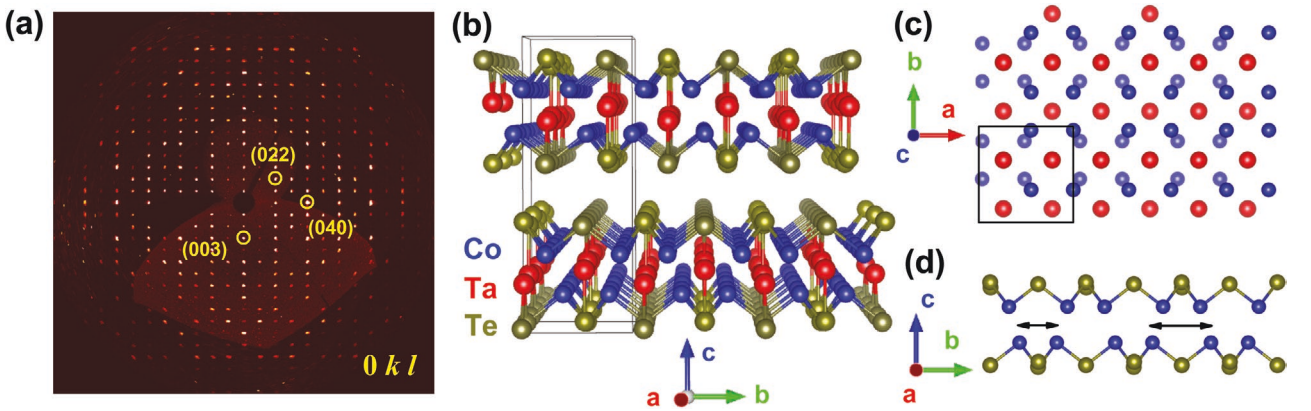

Figure 1. Crystal structure of $TaCo_2Te_2$. a) Indexed precession single crystal X-ray diffraction image along the [0*kl*] direction of a $TaCo_2Te_2$ single crystal. b) The solved crystal structure. c) Each layer consists of two interpenetrating square-nets of Ta atoms and Co dimers in the *ab*-plane. d) The distorted Co chains along the *a*-axis. The black arrows illustrate the changing distance between two consecutive Co atoms within a chain.

© 2021 Wiley-VCH GmbH

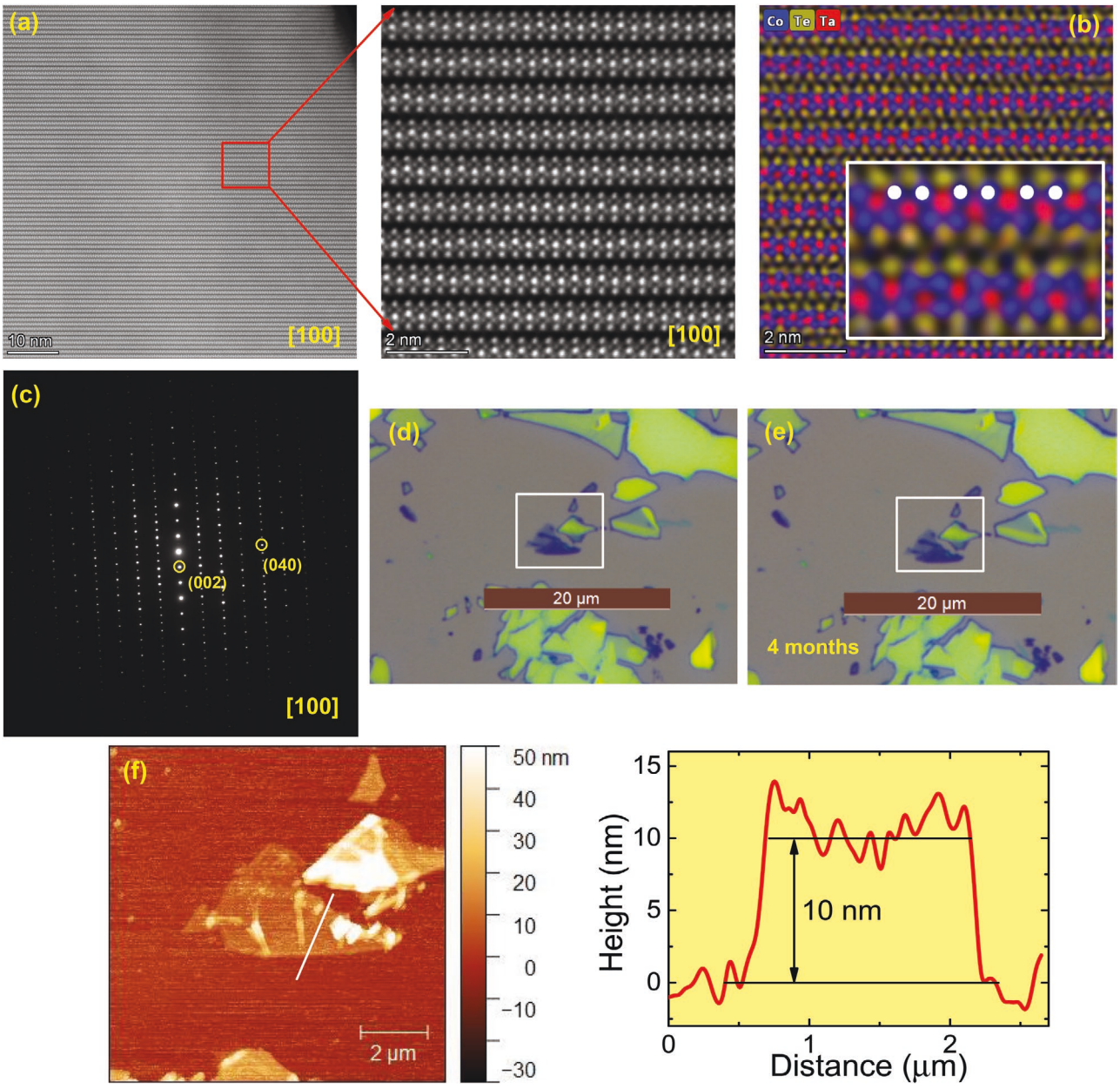

Figure 2. Atomic scale imaging and mechanical exfoliation of $TaCo_2Te_2$ single crystals. a) Extreme high-resolution, high-angle annular dark-field scanning transmission electron microscopy image of a crystal along the *a*-axis, showing the van der Waals gap between the layers. b) Elemental mapping of the image. The inset shows an enlarged view where subsequent Co atoms are highlighted by white points to emphasize the Peierls-distorted structure. c) Selected area electron diffraction pattern along the [100] axis. A typical $TaCo_2Te_2$ thin flake d) immediately after exfoliation and e) after exposure to air for 4 months. f) Atomic force microscopy image of the thin flake (left panel) and the obtained height profile (right panel).

In Figure 2d an optical image of a typical thin flake is highlighted by the white box. This thin flake looks visually unaffected under the optical microscope after exposure to air for at least 4 months (Figure 2e). Nevertheless, we cannot exclude the possibility of microstructural changes due to mild air sensitivity. This is in stark contrast to $GdTe_3$, where fast degradation can be observed under the optical microscope.[27] The demonstrated air stability is remarkable for the sheets, especially for a telluride, as these tend to be very air sensitive.[50,51] Therefore, $TaCo_2Te_2$ is an ideal material for device fabrication. In order to determine the thickness of the flake, we performed atomic force microscopy (AFM), as shown in Figure 2f (left panel). The thinnest part of the flake is ≈10 nm (Figure 2f: right panel). This thickness corresponds to about 11 layers.

2.2. Magnetic Properties of the Bulk Single Crystals

Next, we study the magnetic properties of the $TaCo_2Te_2$ crystals. The temperature (T) dependence of the magnetic susceptibility

© 2021 Wiley-VCH GmbH

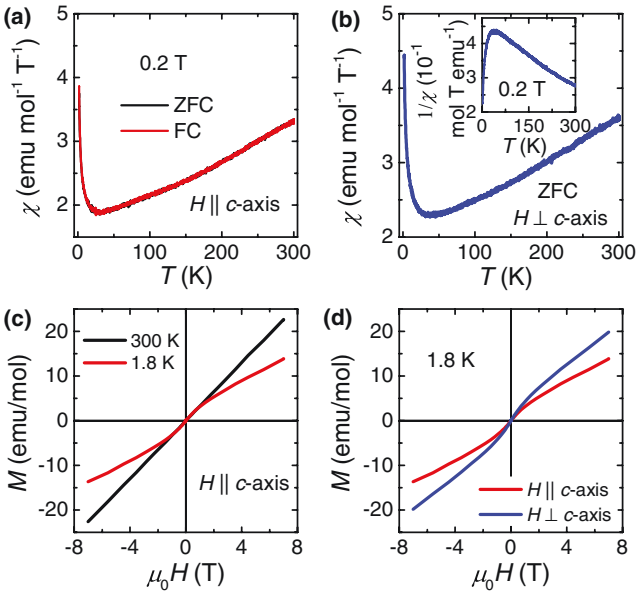

Figure 3. Magnetic properties of the $TaCo_2Te_2$ crystals. a) Temperature dependence of the magnetic susceptibility (χ) under ZFC and FC conditions with the field applied along the *c*-axis. b) χ(*T*) under ZFC with magnetic field applied perpendicular to the *c*-axis. The inset shows the inverse magnetic susceptibility (1/χ) plotted as a function of temperature. c) Magnetic field (*H*) dependence of the magnetization (*M*). d) *M*(*H*) curves at 1.8 K for magnetic field applied along the *c*-axis and along the *ab*-plane.

(χ) is shown in **Figure 3**a in both zero-field-cooled (ZFC) and FC conditions with the field applied along the *c*-axis. The experimental data reveal a rather unusual behavior, where χ(*T*) decreases monotonically from room temperature followed by a sharp increase below ≈14 K without any significant bifurcation between ZFC and FC curves. A similar behavior is observed when the field is applied along the *ab*-plane (Figure 3b). However, the susceptibility is noticeably higher for *H*⊥*c*-axis. The unusual temperature dependence of χ persists up to 400 K (Figure S3a, Supporting Information). This results in a 1/χ(*T*)-plot that is drastically different from that what would be expected for Curie–Weiss behavior (Figure 3b: inset). While we could not identify a clear susceptibility peak corresponding to long-range magnetic ordering down to 1.8 K, the unusual χ versus *T* curve might suggest that magnetic order or fluctuations exist at room temperature. Another interpretation could be the Pauli paramagnetism of the metallic state of $TaCo_2Te_2$. However, we note that in the case of Pauli paramagnetism, the susceptibility should be temperature independent, while in $TaCo_2Te_2$ it gradually increases with temperature. To further rule out Pauli paramagnetism, we compare $TaCo_2Te_2$ to two oxides in which similar magnetic properties have been reported: i) the fractional valence state iridate $La_3Ir_3O_{11}$[52] and ii) the 4d transition metal oxide RuO_2.[53] Both materials are antiferromagnetic at room temperature, with Néel temperatures (T_N) well above 300 K (500–900 K). Unlike $TaCo_2Te_2$, $La_3Ir_3O_{11}$ has a spin-orbit interaction induced Mott insulating state. In this material, strong geometrical frustration prevents long-range magnetic ordering, making it a potential candidate for observing the spin-liquid state.[52] This frustrated structure and competing magnetic exchange interactions within the lattice also lead to non-Curie–Weiss paramagnetism at high temperature.[52] On the other hand, RuO_2 might be the better candidate for comparison, as it is metallic in nature and has negligible correlation effects.[53] The short range antiferromagnetism in RuO_2 originates from a Fermi surface instability.[53] A similar scenario could play out in $TaCo_2Te_2$, as it is Peierls distorted which implies a nesting in the Fermi surface. It is additionally possible that $TaCo_2Te_2$ might start to follow the Curie–Weiss law well above the room temperature. If indeed $TaCo_2Te_2$ has a frustrated magnetic structure, which is not unexpected given the complex arrangement of the Co atoms in each layer, or if it features an instability of the nested Fermi surface, it would be interesting to probe the magnetism with changing layer numbers and in the monolayer.

The other feature of interest in the χ(*T*) plot is the sharp increase at low temperature. In the case of $La_3Ir_3O_{11}$, this increase in χ at low temperature has been proposed to result from isolated Ir ions due to unavoidable defects in the grown crystals. To explore this possibility, in Figure S3b, Supporting Information, we have compared the relative susceptibility curves [χ(*T*)/χ(*T* = 300 K)] for two $TaCo_2Te_2$ crystals from different growth batches. It is evident that the nature and intensity of this enhancement in χ(*T*) is almost identical for these two samples. As the concentration and distribution of structural defects and impurities should be random across different samples from different batches, they cannot produce similar effects in the experimental results. Therefore, this low-temperature enhancement must be an intrinsic property of $TaCo_2Te_2$. The magnetic field (*H*) dependence of the magnetization (*M*) in Figure 3c shows a canted antiferromagnetic behavior at 1.8 K without any signature of saturation up to 7 T. The nature of the *M*(*H*) curve remains similar when the field is applied along the *ab*-plane (Figure 3d). We also observe a clear magnetocrystalline anisotropy between these two crystallographic directions. A similar magnetization behavior for both crystallographic directions as well as the absence of a clear magnetic easy axis further confirms a canted magnetic structure instead of a simple antiferromagnetic spin arrangement between the layers along the *c*-axis. On the other hand, the *M*(*H*) curve resembles either an antiferromagnet or paramagnet at room temperature (Figure 3c).

In order to better understand the nature of the magnetism in $TaCo_2Te_2$, we have performed noncollinear spin-polarized density functional theory calculations, where spin-orbit coupling (SOC) was accounted for (Figure S4, Supporting Information). Without the exact knowledge of the spin structure, a simple picture where Co spins are either parallel (up) or antiparallel (down) to the *c*-axis is assumed. Starting from different possible spin arrangements (either ferromagnetic or antiferromagnetic) of the consecutive Co layers, the magnetic structures are theoretically optimized to obtain the minimum energy solutions. It is found that an antiferromagnetic arrangement yields the most stable ground state with an estimated total energy (E_{total}) lower than that obtained from the calculation without spin-polarization. Note that calculations without spin-polarization will also lead a magnetic structure due to SOC, thus within the framework of density functional theory, a nonmagnetic solution does not exist. The lowest energy magnetic structure consists of canted ferromagnetic layers that are antiferromagnetically

© 2021 Wiley-VCH GmbH

aligned to each other. The energy difference to other magnetic structures is ≈100 meV which is comparable to the energy difference between various magnetic states of other materials, for example in $MnBi_2Te_4$.[54] Hence, the theoretical results also suggest that $TaCo_2Te_2$ is an antiferromagnet. It is interesting to note that all possible magnetic configurations converge to a canted spin structure without a distinct easy axis of magnetization, which further validates our conclusion of a canted antiferromagnetic state in this material. Nonetheless, additional experimental studies are required to validate the theoretical prediction. We know that in vdW materials, anisotropic intralayer and interlayer magnetic interactions can lead to distinct magnetic states in single or few layers as compared to the bulk crystal, which was recently demonstrated for CrI_3 using magneto-optical Kerr effect experiments.[12] Our spin-polarized calculations on a monolayer $TaCo_2Te_2$ indicate that the most stable magnetic configuration of a monolayer is ferromagnetic (Figure S5, Supporting Information). Therefore, a monolayer $TaCo_2Te_2$ has a potential to be an air-stable room-temperature metallic ferromagnet. Studies on the monolayer, as well as layer-dependent magnetism, should be the logical next step to unleash the full potential of this material for functional device applications.

2.3. Electronic Transport Properties

Having established $TaCo_2Te_2$ as an air-stable, antiferromagnetic, exfoliable material, we now turn to the electronic transport properties of bulk $TaCo_2Te_2$ crystals. **Figure 4**a displays the temperature dependent resistivity (ρ_{xx}) with the current along the *a*-axis; a metallic character is observed throughout the measured temperature range, that is, it decreases monotonically from room temperature. The residual resistivity ratio [RRR=ρ_{xx}(300 K)/ρ_{xx}(2 K)] is ≈17, pointing to decent crystal quality. In the low-temperature region below 25 K, ρ_{xx} follows a T^4-behavior (Figure 4a: inset), which is distinct from a quadratic temperature dependence expected from Fermi liquid theory (pure electron–electron scattering), or a T^5-dependence expected for the electron–phonon scattering.[55] We note that T^4-dependence could originate from interband electron–phonon scattering.[55,56]

Upon applying a magnetic field along the *c*-axis, a large, non-saturating magnetoresistance [$MR = \frac{\rho_{xx}(\mu_0 H) - \rho_{xx}(0)}{\rho_{xx}(0)} \times 100\ \%$] is observed (Figure 4b). At 2 K and 9 T, the MR reaches ≈263% and decreases with increasing temperature. The origin of such large MR is much debated, especially in the context of topological semimetals. However, one possible explanation is provided by the semiclassical electron theory for a material with compensated density of the electron- and hole-type carriers.[55] In this scenario, the MR should show a quadratic magnetic field dependence. In $TaCo_2Te_2$, the MR follows a $H^{1.5}$-type relation, which is close but not identical to the expected H^2-dependence for a fully-compensated system. We also measured the directional dependence of this MR by rotating the magnetic field in the *bc*-plane while keeping the current direction along the *a*-axis (Figure 4c: schematic). This measurement configuration ensures that the

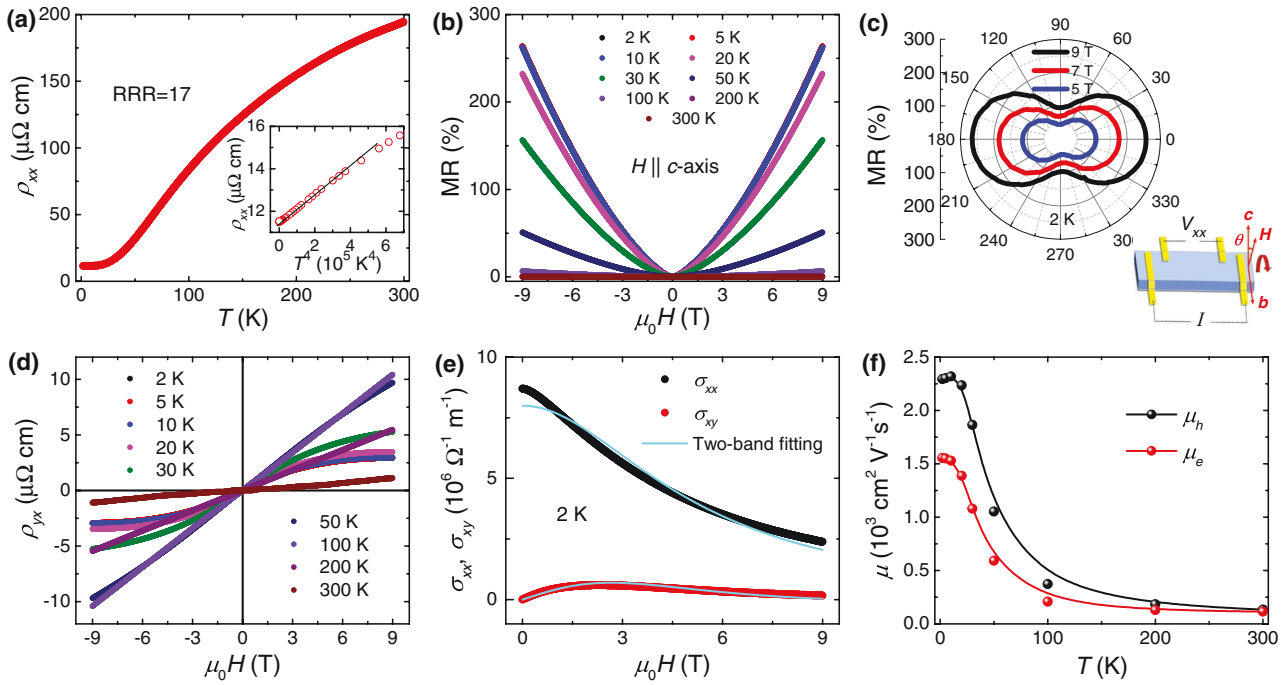

Figure 4. Electronic transport properties of $TaCo_2Te_2$ single crystals. a) Temperature (*T*) dependence of the resistivity (ρ_{xx}) with the current along the *a*-axis. The inset shows the $\rho_{xx} \propto T^4$-type behavior in the low-temperature region. b) Magnetoresistance (MR) at different temperatures with the magnetic field applied along the *c*-axis. c) Directional dependence of the MR at 2 K, when the magnetic field is rotated within the *bc*-plane. Schematic illustrating the experimental configuration. d) Magnetic field dependence of the Hall resistivity (ρ_{yx}) at different temperatures. e) Simultaneous fitting of the longitudinal conductivity (σ_{xx}) and Hall conductivity (σ_{xy}) using the two-band model. f) Temperature dependence of the mobility for electron- (μ_e) and hole-type (μ_h) carriers. The lines are guide to the eye.

© 2021 Wiley-VCH GmbH

current is always perpendicular to the applied magnetic field direction and there is no contribution of the changing Lorentz force in the directional dependence of the MR. The twofold symmetric pattern of the polar plot in Figure 4c reveals the highly anisotropic nature of the Fermi surface, which is expected given the quasi-2D character of the $TaCo_2Te_2$ crystals. Furthermore, several additional weak kinks are observed at angles 17°, 32°, 47°, and 63° (and symmetrically in all of the four quadrants), indicating a complex structure of the Fermi surface.

To gain insight into the nature of the charge carriers, Hall effect measurements were performed. Figure 4d shows the Hall resistivity (ρ_{yx}) as a function of the magnetic field at different temperatures. The nonlinear field dependence of the $\rho_{yx}(H)$ curves confirms the presence of multiple Fermi pockets in $TaCo_2Te_2$. It is important to note that in magnetic materials, the suppression of spin fluctuations with magnetic field plays an important role in the electronic transport properties. It also results in a negative MR. However, the effect of spin scattering is most prominent near the magnetic transition temperature and washes out as we move above or below this ordering temperature. For $TaCo_2Te_2$, as T_N seems to be very high, the contribution of spin scattering in transport properties should be negligible within the measured temperature range (2–300 K). Hence, to analyze the Hall data, we used the conventional two-band model, which takes into account the contributions from both electron and hole-type carriers,[57]

$$\sigma_{xy} = \left[\frac{n_h\mu_h^2}{1+(\mu_h\mu_0 H)^2} - \frac{n_e\mu_e^2}{1+(\mu_e\mu_0 H)^2}\right] e\mu_0 H \quad (1)$$

$$\sigma_{xx} = e\left[\frac{n_h\mu_h}{1+(\mu_h\mu_0 H)^2} + \frac{n_e\mu_e}{1+(\mu_e\mu_0 H)^2}\right] \quad (2)$$

where $\sigma_{xy}=\frac{\rho_{yx}}{\rho_{yx}^2+\rho_{xx}^2}$ and $\sigma_{xx}=\frac{\rho_{xx}}{\rho_{yx}^2+\rho_{xx}^2}$ are Hall conductivity and longitudinal conductivity, respectively. n_h (n_e) and μ_h (μ_e) are hole (electron) density and mobility, respectively. Using the Equations (1) and (2), the $\sigma_{xy}(H)$ and $\sigma_{xx}(H)$ curves are fitted simultaneously for different temperatures. In Figure 4e, one such fitting is shown for a representative temperature. From the extracted fitting parameters, we find the electron and hole density to be $1.442(9) \times 10^{20}$ and $1.202(6) \times 10^{20}$ cm^{-3}, respectively. These values reveal that $TaCo_2Te_2$ is a nearly-compensated semimetal, which is consistent with the nature of the MR curves as already discussed. At 2 K, the obtained electron and hole mobilities are $1.553(9) \times 10^3$ and $2.293(11) \times 10^3$ cm^2 V^{-1} s^{-1}, respectively. Although these values are one order of magnitude smaller than the highest quality $GdTe_3$ crystals,[27] they are still very high and comparable to several topological semimetals.[58,59] In **Table 1**, we have compared the carrier mobility for $TaCo_2Te_2$ with that for different magnetic layered compounds. It is evident that this compound is a rare air-stable, magnetic vdW system which also hosts high-mobility charge carriers. As Figure 4f illustrates, the mobility for both types of carriers decreases with increasing temperature.

As the $TaCo_2Te_2$ crystals are cooled below 2 K, we observe prominent Shubnikov–de Haas (SdH) quantum oscillations in the MR for magnetic field along the *c*-axis. The appearance of the SdH oscillations also suggests a long mean free path and hence high mobility of the charge carriers. After subtracting a smooth background from the experimental data, the extracted oscillatory part ($\Delta\rho_{xx}$) of the resistivity is plotted as a function of the inverse magnetic field in **Figure 5** for two different temperatures. The corresponding fast Fourier transform spectrum (shown in the inset) reveals three oscillation frequencies (F), 55, 154, and 208 T, thus further confirming the presence of multiple Fermi pockets in $TaCo_2Te_2$. From these quantum oscillation frequencies, we can calculate the extremum cross-sectional area (A_F) of the Fermi surface perpendicular to the magnetic field direction by using the Onsager relation, $F = (\phi_0/2\pi^2)A_F$, where ϕ_0 is the magnetic flux quantum. The obtained cross-sectional areas are 5.24×10^{-3}, 14.68×10^{-3}, and 19.82×10^{-3} $Å^{-2}$, respectively.

Table 1. Comparison of the carrier mobility in bulk single crystals of metallic, magnetic layered compounds. We have also listed the magnetic state and whether it is an air-stable vdW material.

Material	Magnetic state	vdW?	Air-stable?	Mobility [$cm^2V^{-1}s^{-1}$]	Reference
$GdTe_3$	Antiferromagnetic	Yes	No	23500-61200	[27]
$NdTe_3$	Antiferromagnetic	Yes	No	60000	[28]
$EuMnBi_2$	Antiferromagnetic	No	Unknown	14000	[60]
$TbTe_3$	Antiferromagnetic	Yes	No	2000-8000	[61]
$YbMnSb_2$	Antiferromagnetic	No	Yes	1310-6538	[62]
$TaCo_2Te_2$	Canted antiferromagnetic	Yes	Yes	1553-2293	This work
$BaMnSb_2$	Antiferromagnetic	No	Unknown	1300	[63]
$BaFe_2As_2$	Antiferromagnetic	No	Yes	1130	[64]
$Sr_{1-y}Mn_{1-z}Sb_2$	Ferromagnetic	No	No	570	[65]
$CaMnBi_2$	Antiferromagnetic	No	Unknown	488	[66]
$SrMnBi_2$	Antiferromagnetic	No	No	250	[67]
$Co_3Sn_2S_2$	Ferromagnetic	No	Yes	≈100	[68]
Fe_3GeTe_2	Ferromagnetic	Yes	Yes	≈2.8	[23]

© 2021 Wiley-VCH GmbH

3. Outlook and Conclusions

We demonstrate that chemical principles can be used to find 2D materials with rare combination of physical properties. Our strategy, based on the presence of a structural distortion in combination with a layered structure and the presence of typically magnetic elements, has proven fruitful for finding a new, air-stable, high-mobility magnetic vdW material. It is worth noting that our chemical reasoning led us to a 2D material that was overlooked in extended computational searches, as $TaCo_2Te_2$ does not appear in the 2D materials database.[2] The results of our band structure calculations (Figure S6a, Supporting Information) for bulk $TaCo_2Te_2$ reveal that the Fermi surface of this material is very complex as a large number of bands reside at the Fermi energy. Thus this material might have been considered unappealing due to the messy band structure. The steep nature of the bands, however, could give an indication of the high-mobility carriers. Our theoretical calculations further predict that the metallic character of $TaCo_2Te_2$ persists down to the monolayer limit (Figure S6b, Supporting Information).

To conclude, we showed that the single-crystalline vdW compound $TaCo_2Te_2$ is a great candidate for 2D device fabrication. This material has large vdW gap and hence the bulk crystals can easily be exfoliated to few layers. Moreover, the thin flakes are robust in air for at least 4 months as observed in optical microscopy. Magnetization measurements show canted antiferromagnetic behavior at low temperature with possible magnetic frustration. $TaCo_2Te_2$ is metallic and shows a large, nonsaturating, anisotropic MR, which possibly originates from the nearly compensated electron and hole density in this material. Hall effect measurements reveal high mobility for both types of charge carriers. We have observed quantum oscillations in the MR data, which also confirm the presence of multiple Fermi pockets. Thus, $TaCo_2Te_2$ is a rare magnetic vdW compound, which offers a range of unique functionalities highly desired for low-dimensional device technology.

4. Experimental Section

Single Crystal Growth and Determination of the Stoichiometry: Single crystals of $TaCo_2Te_2$ were grown with chemical vapor transport using iodine as transport agent. First, the polycrystalline powder was prepared in a solid state reaction. Elemental Ta (Sigma-Aldrich 99.99%), Co (Sigma-Aldrich 99.9%), Te (Sigma-Aldrich 99.999%) were mixed in molar ratio and sealed in a evacuated quartz tube, which was then heated to 900 °C for 3 days. Next, the resulting powder was mixed with iodine (Sigma-Aldrich 99.99%) and sealed in another quartz tube under vacuum. The tube was placed in a gradient furnace for 7 days keeping the hotter end with the powder at 950 °C and the other end of the tube at 850 °C. After cooling down, plate-like crystals were mechanically extracted from the colder end of the quartz tube. The stoichiometry of the grown crystals was checked using EDX in a Verios 460 SEM operating at 15 kV and equipped with an Oxford EDX detector.

X-Ray Diffraction Measurements: The SCXRD measurements were performed using a Bruker D8 VENTURE diffractometer fitted with a PHOTON III CPAD detector and graphite-monochromatized Mo-K_α radiation source. Raw data were corrected for background, polarization, Lorentz factors, and multiscan absorption. Structure refinements were performed using the OLEX2 software package.

Scanning/Transmission Electron Microscopy: TEM thin lamella for microstructure characterization were prepared by focused ion beam cutting via a FEI Helios NanoLab 600 dual beam system (FIB/SEM). Conventional TEM imaging, atomic resolution HAADF-STEM imaging, and atomic-level EDX mapping were performed on a double Cs-corrected FEI Titan Cubed Themis 300 scanning/transmission electron microscope equipped with an X-FEG source operated at 300 kV and Super-X EDX system. The microscope was equipped with a Gatan Quantum SE/963 P post-column energy filter for energy filtered TEM. The high-resolution STEM images were processed using the Gatan Microscopy Suite (GMS 3.4.3) software. The electron diffraction simulations were performed using the CrystalMaker and SingleCrystal software package.

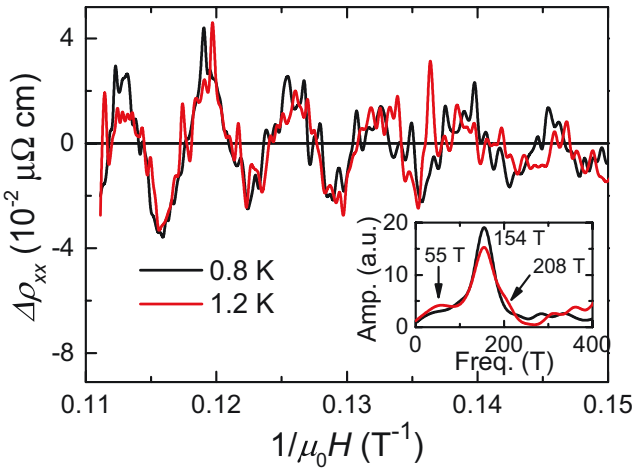

Figure 5. SdH quantum oscillations in the $TaCo_2Te_2$ crystals. The inset shows the corresponding fast Fourier transform spectrum.

AFM: The AFM of the thin flakes was performed using a Bruker NanoMan AFM. The raw data were processed by Gwyddion software package.

Electronic Transport and Magnetization Measurements: The electronic transport measurements of the $TaCo_2Te_2$ crystals were done in a physical property measurement system (Quantum Design) using the ac-transport option. Electrical contacts were attached on the crystals in four-probe configuration using gold wires and silver paste. For achieving sample temperatures lower than 1.8 K, a dilution refrigerator insert was used. The magnetization data were collected in a SQUID-VSM MPMS3 (Quantum Design).

Band Structure Calculations: Band structure calculations were carried out using VASP 5.4.4. software.[69,70] Geometry of bulk $TaCo_2Te_2$ was taken from the crystallographic data, while a monolayer was created by increasing the distance between layers from 3.8782 to 24.2748 Å. Geometries were not relaxed. Band structures were calculated using the strongly constrained and appropriately normed semilocal density functional[71] for exchange and correlation, and Ta_pv, Te, and Co projector augmented wave potentials.[72,73] Γ-centered $8 \times 8 \times 3$ and 7×7 Monkhorst–Pack meshes[74] were used to obtain wave-functions of the bulk compound and the monolayer, respectively. To capture magnetic properties, noncollinear calculations were performed with spin-polarization and SOC,[75] where the spin quantization axis was chosen to be orthogonal to layers (parallel to the c-axis).

Supporting Information

Supporting Information is available from the Wiley Online Library or from the author.

Acknowledgements

This work was supported by the Gordon and Betty Moore Foundation's EPIQS initiative through Grant GBMF9064, the David and Lucile

© 2021 Wiley-VCH GmbH

Packard foundation, the Sloan foundation, and the Princeton Catalysis Initiative (PCI). The authors acknowledge the use of Princeton's Imaging and Analysis Center (IAC), which is partially supported by the Princeton Center for Complex Materials (PCCM), a National Science Foundation (NSF) Materials Research Science and Engineering Center (MRSEC; DMR-2011750). The authors acknowledge the support from the University of California Santa Barbara Quantum Foundry, funded by the NSF (DMR-1906325). The research reported here also made use of shared facilities of the UC Santa Barbara Materials Research Science and Engineering Center (NSF DMR-1720256). Y.M.O is supported by the NSF Graduate Research Fellowship Program under Grant No. DGE-1650114.

Conflict of Interest

The authors declare no conflict of interest.

Data Availability Statement

The data that support the findings of this study are available from the corresponding author upon reasonable request.

Keywords

antiferromagnetism, high mobility, Peierls distortion, van der Waals material

Received: September 3, 2021
Revised: October 25, 2021
Published online: November 10, 2021

[1] K. S. Novoselov, A. Mishchenko, A. Carvalho, A. H. Castro Neto, *Science* **2016**, *353*, aac9439.
[2] N. Mounet, M. Gibertini, P. Schwaller, D. Campi, A. Merkys, A. Marrazzo, T. Sohier, I. E. Castelli, A. Cepellotti, G. Pizzi, N. Marzari, *Nat. Nanotechnol.* **2018**, *13*, 246.
[3] X. Xi, Z. Wang, W. Zhao, J.-H. Park, K. T. Law, H. Berger, L, Forró, J. Shan, K. F. Mak, *Nat. Phys.* **2016**, *12*, 139.
[4] Y. Qi, P. G. Naumov, M. N. Ali, C. R. Rajamathi, W. Schnelle, O. Barkalov, M. Hanfland, S.-C. Wu, C. Shekhar, Y. Sun, V. Süß, M. Schmidt, U. Schwarz, E. Pippel, P. Werner, R. Hillebrand, T. Förster, E. Kampert, S. Parkin, R. J. Cava, C. Felser, B. Yan, S. A. Medvedev, *Nat. Commun.* **2016**, *7*, 11038.
[5] G. H. Han, D. L. Duong, D. H. Keum, S. Joon Yun, Y. H. Lee, *Chem. Rev.* **2018**, *118*, 6297.
[6] Q. H. Wang, K. Kalantar-Zadeh, A. Kis, J. N. Coleman, M. S. Strano, *Nat. Nanotechnol.* **2012**, *7*, 699.
[7] X. Zhou, X. Hu, J. Yu, S. Liu, Z. Shu, Q. Zhang, H. Li, Y. Ma, H. Xu, T. Zhai, *Adv. Funct. Mater.* **2018**, *28*, 1706587.
[8] T. Gao, Q. Zhang, L. Li, X. Zhou, L. Li, H. Li, T. Zhai, *Adv. Opt. Mater.* **2018**, *6*, 1800058.
[9] K. S. Burch, D. Mandrus, J.-G. Park, *Nature* **2018**, *563*, 47.
[10] S. Kezilebieke, M. N. Huda, V. Vaño, M. Aapro, S. C. Ganguli, O. J. Silveira, S. Głodzik, A. S. Foster, T. Ojanen, P. Liljeroth, *Nature* **2020**, *588*, 424.
[11] C. Tang, Z. Zhang, S. Lai, Q. Tan, W.-B. Gao, *Adv. Mater.* **2020**, *32*, 1908498.
[12] B. Huang, G. Clark, E. Navarro-Moratalla, D. R. Klein, R. Cheng, K. L. Seyler, D. Zhong, E. Schmidgall, M. A. McGuire, D. H. Cobden, W. Yao, D. Xiao, P. Jarillo-Herrero, X. Xu, *Nature* **2017**, *546*, 270.
[13] B. Huang, G. Clark, D. R. Klein, D. MacNeill, E. Navarro-Moratalla, K. L. Seyler, N. Wilson, M. A. McGuire, D. H. Cobden, D. Xiao, W. Yao, P. Jarillo-Herrero, X. Xu, *Nat. Nanotechnol.* **2018**, *13*, 544.
[14] C. Gong, L. Li, Z. Li, H. Ji, A. Stern, Y. Xia, T. Cao, W. Bao, C. Wang, Y. Wang, Z. Q. Qiu, R. J. Cava, S. G. Louie, J. Xia, X. Zhang, *Nature* **2017**, *546*, 265.
[15] T. Zhang, Y. Wang, H. Li, F. Zhong, J. Shi, M. Wu, Z. Sun, W. Shen, B. Wei, W. Hu, X. Liu, L. Huang, C. Hu, Z. Wang, C. Jiang, S. Yang, Q.-M. Zhang, Z. Qu, *ACS Nano* **2019**, *13*, 11353.
[16] X. Wang, J. Tang, X. Xia, C. He, J. Zhang, Y. Liu, C. Wan, C. Fang, C. Guo, W. Yang, Yao Guang, X. Zhang, H. Xu, J. Wei, M. Liao, X. Lu, J. Feng, X. Li, Y. Peng, H. Wei, R. Yang, D. Shi, X. Zhang, Z. Han, Z. Zhang, G. Zhang, G. Yu, X. Han, *Sci. Adv.* **2019**, *5*, eaaw8904.
[17] D. Ghazaryan, M. T. Greenaway, Z. Wang, V. H. Guarochico-Moreira, I. J. Vera-Marun, J. Yin, Y. Liao, S. V. Morozov, O. Kristanovski, A. I. Lichtenstein, M. I. Katsnelson, F. Withers, A. Mishchenko, L. Eaves, A. K. Geim, K. S. Novoselov, A. Misra, *Nat. Electron.* **2018**, *1*, 344.
[18] X. Cai, T. Song, N. P. Wilson, G. Clark, M. He, X. Zhang, T. Taniguchi, K. Watanabe, W. Yao, D. Xiao, M. A. McGuire, D. H. Cobden, X. Xu, *Nano Lett.* **2019**, *19*, 3993.
[19] D. Weber, L. M. Schoop, V. Duppel, J. M. Lippmann, J. Nuss, B. V. Lotsch, *Nano Lett.* **2016**, *16*, 3578.
[20] J.-U. Lee, S. Lee, J. H. Ryoo, S. Kang, T. Y. Kim, P. Kim, C.-H. Park, J.-G. Park, H. Cheong, *Nano Lett.* **2016**, *16*, 7433.
[21] T. Song, X. Cai, M. W.-Y. Tu, X. Zhang, B. Huang, N. P. Wilson, K. L. Seyler, L. Zhu, T. Taniguchi, K. Watanabe, M. A. McGuire, D. H. Cobden, D. Xiao, W. Yao, X. Xu, *Science* **2018**, *360*, 1214.
[22] Z.-Z. Lin, X. Chen, *Adv. Electron. Mater.* **2020**, *6*, 6.
[23] Y. Wang, C. Xian, J. Wang, B. Liu, L. Ling, L. Zhang, L. Cao, Z. Qu, Y. Xiong, *Phys. Rev. B* **2017**, *96*, 96.
[24] J. Seo, D. Y. Kim, E. S. An, K. Kim, G.-Y. Kim, S.-Y. Hwang, D. W. Kim, B. G. Jang, H. Kim, G. Eom, S. Y. Seo, R. Stania, M. Muntwiler, J. Lee, K. Watanabe, T. Taniguchi, Y. J. Jo, J. Lee, B. I. Min, M. H. Jo, H. W. Yeom, S.-Y. Choi, J. H. Shim, J. S. Kim, *Sci. Adv.* **2020**, *6*, eaay8912.
[25] N. Ru, I. R. Fisher, *Phys. Rev. B* **2006**, *73*, 73.
[26] N. Ru, J.-H. Chu, I. R. Fisher, *Phys. Rev. B* **2008**, *78*, 78.
[27] S. Lei, J. Lin, Y. Jia, M. Gray, A. Topp, G. Farahi, S. Klemenz, T. Gao, F. Rodolakis, J. L. McChesney, C. R. Ast, A. Yazdani, K. S. Burch, S. Wu, N. P. Ong, L. M. Schoop, *Sci. Adv.* **2020**, *6*, eaay6407.
[28] K. J. Dalgaard, S. Lei, S. Wiedmann, M. Bremholm, L. M. Schoop, *Phys. Rev. B* **2020**, *102*, 102.
[29] L. Liao, Y.-C. Lin, M. Bao, R. Cheng, J. Bai, Y. Liu, Y. Qu, K. L. Wang, Y. Huang, X. Duan, *Nature* **2010**, *467*, 305.
[30] R. O. Dillon, I. L. Spain, J. A. Woollam, W. H. Lowrey, *J. Phys. Chem. Solid* **1978**, *39*, 907.
[31] Y. Akahama, S. Endo, S.-i. Narita, *J. Phys. Soc. Jpn.* **1983**, *52*, 2148.
[32] K. S. Novoselov, V. I. Fal'ko, L. Colombo, P. R. Gellert, M. G. Schwab, K. Kim, *Nature* **2012**, *490*, 192.
[33] K. Kostarelos, K. S. Novoselov, *Nat. Nanotechnol.* **2014**, *9*, 744.
[34] X. Li, M. Rui, J. Song, Z. Shen, H. Zeng, *Adv. Funct. Mater.* **2015**, *25*, 4929.
[35] A. Castellanos-Gomez, *J. Phys. Chem. Lett.* **2015**, *6*, 4280.
[36] B. Li, C. Lai, G. Zeng, D. Huang, L. Qin, M. Zhang, M. Cheng, X. Liu, H. Yi, C. Zhou, F. Huang, S. Liu, Y. Fu, *Small* **2019**, *15*, 15.
[37] Y. Cao, V. Fatemi, S. Fang, K. Watanabe, T. Taniguchi, E. Kaxiras, P. Jarillo-Herrero, *Nature* **2018**, *556*, 43.
[38] Y. Cao, V. Fatemi, A. Demir, S. Fang, S. L. Tomarken, J. Y. Luo, J. D. Sanchez-Yamagishi, K. Watanabe, T. Taniguchi, E. Kaxiras, R. C. Ashoori, P. Jarillo-Herrero, *Nature* **2018**, *556*, 80.
[39] A. L. Sharpe, E. J. Fox, A. W. Barnard, J. Finney, K. Watanabe, T. Taniguchi, M. A. Kastner, D. Goldhaber-Gordon, *Science* **2019**, *365*, 605.
[40] S. Bhatti, R. Sbiaa, A. Hirohata, H. Ohno, S. Fukami, S. N. Piramanayagam, *Mater. Today* **2017**, *20*, 530.

© 2021 Wiley-VCH GmbH

[41] S. Klemenz, S. Lei, L. M. Schoop, *Ann. Rev. Mater. Res.* **2019**, *49*, 185.
[42] J. F. Khoury, L. M. Schoop, *Trends Chem.* **2021**, *3*, 700.
[43] A. Castellanos-Gomez, L. Vicarelli, E. Prada, J. O. Island, K. L. Narasimha-Acharya, S. I Blanter, D. J. Groenendijk, M. Buscema, G. A. Steele, *2D Mater.* **2014**, *1*, 025001.
[44] L. M. Schoop, F. Pielnhofer, B. V. Lotsch, *Chem. Mater.* **2018**, *30*, 3155.
[45] W. Tremel, *J. Chem. Soc., Chem. Commun* **1991**, *1991*, 1405.
[46] W. Tremel, *Angew. Chem., Int. Ed.* **1992**, *31*, 217.
[47] J.-P. Pouget, *C. R. Phys.* **2016**, *17*, 332.
[48] A. Purbawati, J. Coraux, J. Vogel, A. Hadj-Azzem, N.-J. Wu, N. Bendiab, D. Jegouso, J. Renard, L. Marty, V. Bouchiat, A. Sulpice, L. Aballe, M. Foerster, F. Genuzio, A. Locatelli, T. O. Menteş, Z. V. Han, X. Sun, M. Núñez-Regueiro, N. Rougemaille, *ACS Appl. Mater. Interfaces* **2020**, *12*, 30702.
[49] Y. Liu, Y. Huang, X. Duan, *Nature* **2019**, *567*, 323.
[50] F. Ye, J. Lee, J. Hu, Z. Mao, J. Wei, P. X.-L. Feng, *Small* **2016**, *12*, 5802.
[51] G. Mirabelli, C. McGeough, M. Schmidt, E. K. McCarthy, S. Monaghan, I. M. Povey, M. McCarthy, F. Gity, R. Nagle, G. Hughes, A. Cafolla, P. K. Hurley, R. Duffy, *J. App. Phys.* **2016**, *120*, 120.
[52] J. Yang, J. R. Wang, W. L. Zhen, L. Ma, L. S. Ling, W. Tong, C. J. Zhang, L. Pi, W. K. Zhu, *Phys. Rev. B* **2019**, *100*, 100.
[53] T. Berlijn, P. C. Snijders, O. Delaire, H.-D. Zhou, T. A. Maier, H.-B. Cao, S.-X. Chi, M. Matsuda, Y. Wang, M. R. Koehler, P. R. C. Kent, H. H. Weitering, *Phys. Rev. Lett.* **2017**, *118*, 118.
[54] D. Zhang, M. Shi, T. Zhu, D. Xing, H. Zhang, J. Wang, *Phys. Rev. Lett.* **2019**, *122*, 122.
[55] J. M. Ziman, *Electrons and Phonons: The Theory of Transport Phenomena in Solids*, Classics Series, Oxford University Press, New York **2001**.
[56] R. Singha, A. K. Pariari, B. Satpati, P. Mandal, *Proc. Natl. Acad. Sci. U. S. A.* **2017**, *114*, 2468.
[57] C. M. Hurd, *The Hall Effect in Metals and Alloys*, Plenum Press, New York **1972**.
[58] M. Novak, S. Sasaki, K. Segawa, Y. Ando, *Phys. Rev. B* **2015**, *91*, 041203(R).
[59] R. Singha, A. Pariari, B. Satpati, P. Mandal, *Phys. Rev. B* **2017**, *96*, 96.
[60] H. Masuda, H. Sakai, M. Tokunaga, Y. Yamasaki, A. Miyake, J. Shiogai, S. Nakamura, S. Awaji, A. Tsukazaki, H. Nakao, Y. Murakami, T.-h. Arima, Y. Tokura, S. Ishiwata, *Sci. Adv.* **2016**, *2*, e1501117.
[61] Y. Xing, Y. Li, Z. Yang, Z. Wang, P. Yang, J. Ge, Y. Liu, Y. Liu, T. Luo, Y. Tang, J. Wang, *J. Appl. Phys.* **2020**, *128*, 128.
[62] Y.-Y. Wang, S. Xu, L.-L. Sun, T.-L. Xia, *Phys. Rev. Mater.* **2018**, *2*, 021201(R).
[63] J. Liu, J. Hu, H. Cao, Y. Zhu, A. Chuang, D. Graf, D. J. Adams, S. M. A. Radmanesh, L. Spinu, I. Chiorescu, Z. Mao, *Sci. Rep.* **2016**, *6*, 6.
[64] H.-H. Kuo, J.-H. Chu, S. C. Riggs, L. Yu, P. L. McMahon, K. D. Greve, Y. Yamamoto, J. G. Analytis, I. R. Fisher, *Phys. Rev. B* **2011**, *84*, 84.
[65] J. Y. Liu, J. Hu, Q. Zhang, D. Graf, H. B. Cao, S. M. A. Radmanesh, D. J. Adams, Y. L. Zhu, G. F. Cheng, X. Liu, W. A. Phelan, J. Wei, M. Jaime, F. Balakirev, D. A. Tennant, J. F. DiTusa, I. Chiorescu, L. Spinu, Z. Q. Mao, *Nat. Mater.* **2017**, *16*, 905.
[66] A. Wang, D. Graf, L. Wu, K. Wang, E. Bozin, Y. Zhu, C. Petrovic, *Phys. Rev. B* **2016**, *94*, 94.
[67] J. Park, G. Lee, F. Wolff-Fabris, Y. Y. Koh, M. J. Eom, Y. K. Kim, M. A. Farhan, Y. J. Jo, C. Kim, J. H. Shim, J. S. Kim, *Phys. Rev. Lett.* **2011**, *107*, 107.
[68] J. Shen, Q. Yao, Q. Zeng, H. Sun, X. Xi, G. Wu, W. Wang, B. Shen, Q. Liu, E. Liu, *Phys. Rev. Lett.* **2020**, *125*, 125.
[69] G. Kresse, J. Furthmüller, *Comput. Mater. Sci.* **1996**, *6*, 6.
[70] G. Kresse, J. Furthmüller, *Phys. Rev. B* **1996**, *54*, 54.
[71] J. Sun, A. Ruzsinszky, J. P. Perdew, *Phys. Rev. Lett.* **2015**, *115*, 115.
[72] P. E. Blöchl, *Phys. Rev. B* **1994**, *50*, 50.
[73] G. Kresse, D. Joubert, *Phys. Rev. B* **1999**, *59*, 59.
[74] H. J. Monkhorst, J. D. Pack, *Phys. Rev. B* **1976**, *13*, 13.
[75] S. Steiner, S. Khmelevskyi, M. Marsmann, G. Kresse, *Phys. Rev. B* **2016**, *93*, 93.

© 2021 Wiley-VCH GmbH